ACS APPLIED MATERIALS & INTERFACES

www.acsami.org

Research Article

Beyond Capacitance Ratio: Electrolyte Voltage Division and a New Impedance Model for Organic Electrochemical Transistors

Qinyu Hu, Hangyu Li, Shengkai Sun, Viviana Rincón Montes, Sven Ingebrandt, Francesca Santoro, Andreas Offenhäusser, and Dirk Mayer*

Cite This: https://doi.org/10.1021/acsami.6c09414

Read Online

ACCESS | Metrics & More | Article Recommendations | Supporting Information

ABSTRACT: Organic electrochemical transistors (OECTs) can be optimized by tuning the gate-channel capacitance ratio via geometry or materials. However, electrolyte properties also critically influence performance, which is a phenomenon unexplained by capacitive models alone. This study demonstrates that varying electrolyte concentration modulates the on-state current (I_{on}), the off-state current (I_{off}), the on–off ratio (I_{on}/I_{off}), and the threshold voltage (V_T). We propose a new impedance-based model incorporating both capacitive coupling and resistive voltage division across the electrolyte to explain these effects. This model successfully predicts and verifies a frequency-dependent V_T shift under high-frequency signals. Leveraging this insight, we demonstrate that appropriately increasing the gate DC bias compensates for this shift, thereby enhancing transconductance in high-frequency applications.

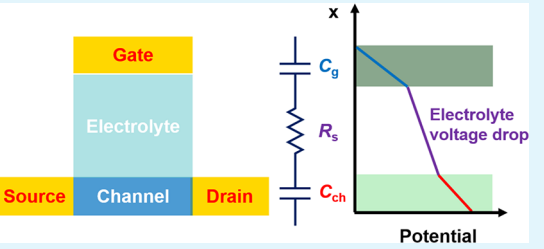

KEYWORDS: *organic electrochemical transistor, threshold voltage, transconductance, electrolyte, frequency*

1. INTRODUCTION

Organic electrochemical transistors (OECTs) utilizing organic mixed ionic-electronic conductors (OMIECs) have gained significant attention due to their capability to act as ionic-to-electronic transducers.[1,2] A typical OECT configuration comprises three terminals, source, drain, and gate, with a conjugated polymer channel bridging the source and drain. The device operates by applying a drain-source voltage (V_{DS}) across the channel to generate an output drain current (I_D). The application of a gate voltage (V_{GS}) modulates the penetration of ions from the electrolyte into the polymer bulk, thereby shifting the channel's doping state and electrical conductivity.[1,3] Because this doping process occurs throughout the entire volume of the channel—rather than being confined to a thin interface—OECTs exhibit remarkably high transconductance values (g_m). This high g_m enables the detection of minute gate voltage fluctuations through substantial changes in I_D, making OECTs ideal for on-site signal amplification.[4−6] Furthermore, the diverse palette of available organic semiconducting materials allows OECTs to be engineered with mechanical stretchability,[7] low interfacial stiffness for soft mechanical contact,[8] and inherent biocompatibility.[9] The volumetric nature of the charge transport within these devices simplifies the fabrication process, enabling cost-effective and scalable manufacturing techniques such as inkjet printing,[10−12] laser patterning,[13,14] and the development of sustainable substrates like wood-based OECTs.[15] Collectively, these advantages have established OECTs as versatile tools in a wide range of cutting-edge applications, including neural interfaces,[16,17] chemical and biological sensors,[18,19] integrated circuits,[20,21] and neuromorphic computing devices.[22−24] Most notably, within the sensing domain, the recent technology roadmap[25] reaffirms that the seamless convergence of these very traits, such as high sensitivity, biocompatibility, and manufacturing efficiency, makes organic transistor-based biosensors a versatile platform for next-generation interactive electronics.

The performance of the OECTs critically depends on the device layout and in particular on the channel. Bernards and Malliaras established the model bridging the channel length (L) and width (W) with the drain current.[3] Rivnay et al. found that the thickness of the channel can tune the performance of OECTs.[26] In the model from Rivnay et al.,[26] the width of the channel and the thickness of the channel (d) are proportional to I_D or g_m, while the length of the channel is inversely proportional to them. However, some researchers found that the gate, which has not appeared directly in this model, impacts OECT performance as well. Tan et al. reported that chemically doped polymer gates can tune the threshold voltage of OECTs.[27] Blom et al. reported that thicker poly(3,4-ethylenedioxythiophene) polystyrene sulfonate (PEDOT:PSS) gates show stronger gating efficiency than their thinner

Received: May 8, 2026
Revised: June 29, 2026
Accepted: July 7, 2026

counterpart.[28] Cicoira et al. reported that varying the gate area can tune the response of their OECT sensors.[29] In their findings, the capacitance ratio $[C_g/(C_g + C_{ch})]$, (capacitance of the gate (C_g) and capacitance of the channel (C_{ch})) plays the critical role. The changes in the capacitance ratio leads to changes in the other performance features, including I_D, g_m, and further sensing ability.[28,30,31] Besides the influence of the capacitance, the electrolyte is also viewed to change the performance of OECT. Lin et al. pointed out that the type of ion in the electrolyte could change the effective V_g of OECTs, and ions with one valence could play a more important role than ions with two or more valencies.[32] Romele et al. also observed that higher ionic concentrations could shift the transfer curve of OECTs to negative potentials.[33] In addition, chemical component variations within the electrolyte could induce profound morphological rearrangements and even conformational transitions, which drastically alter the charge transport properties.[34] Although the influence of the electrolyte is repeatedly observed, none of the prior work established a theory capable of describing the performance changes by varying capacitance ratio and electrolyte composition together.

In this paper, the influence of the electrolyte concentration on the OECT performance is confirmed and explained. I_D and V_T can be changed by tuning the concentration of the electrolyte of OECTs with nearly fixed capacitance ratio. Electrolyte resistance, which has been widely recognized as a dominant factor limiting the transient switching speed of OECTs via the ionic RC time constant[35] but surprisingly overlooked in classical capacitance ratio theories, stands as the primary factor driving the concentration-dependent shift in V_T. A new theory is derived, which utilizes the impedance instead of the capacitance to explain both the influence of the electrolyte concentration and the capacitance, simultaneously. This theory proposes that high frequency signals increase the V_T, which is also confirmed by experiments. An operation point tuning strategy is proposed as a new method to enhance the high-frequency amplification ability of OECTs.

2. RESULTS AND DISCUSSION

All organic electrochemical transistor devices in this work were fabricated on a 5-μm-thick parylene-C (PaC) film, a biocompatible material, supported by a quartz substrate (Figure 1a). The channel between the source and drain consisted of PEDOT:PSS (Figure S2a), a widely studied mixed ion–electron conductor with high electronic and ionic mobility and large transconductance. 3-Glycidoxypropyltrimethoxysilane (GOPS) and dimethyl sulfoxide (DMSO) were added to the polymer to improve the mechanical stability and the electrical conductivity, respectively.[36,37] A transparent glass ring was used to define the electrolyte reservoir on an OECT (Figure S1a), and a chip test socket was employed to contact the metal pads of the chip with its contact pins, which utilized the wire connections to increase measurement efficiency (Figure S1b). During the electrical characterization, the source contact was grounded, while voltages were applied to the gate (V_{GS}) and the drain (V_{DS}). Optical images and device geometry are shown in Figure 1b. All electrodes were made from gold and photolithographically patterned. A second 5-μm-thick PaC layer passivated the electrode edges, enhancing the device stability and lifetime. Figure 1c illustrates the operating mechanism of the p-type depletion-mode PEDOT:PSS based OECT. Under negative gate bias, anions migrate into the channel with minimal impact on the drain current, maintaining a hole-conducting on state. Under positive gate bias, cations penetrate the channel and bind with PSS^- to form PSSM (Figure S2b), reducing $PEDOT^+$ to $PEDOT^0$. This dedoping process lowers the hole concentration and diminishes I_D, corresponding to the off state. During all the measurements, a constant negative V_{DS} was applied to facilitate ion transport. The gate-voltage-dependent doping modulation is reflected in the transfer characteristics (I_D–V_{GS}), Figure 1d. As V_{GS} is swept from –0.4 to 1 V, the device transitions from the on to off state, with I_D decreasing from I_{on} to I_{off}. The transconductance ($g_m = \partial I_D/\partial V_{GS}$) exhibits a clear maximum (peak g_m), indicating the gate voltage at which the device provides maximum amplification. The V_T was extracted from the transfer curve following the maximum transconductance method as described in Figure S3. Output characteristics, obtained by sweeping V_{DS} at fixed V_{GS}, are shown in Figure 1e. Increasing V_{GS} from –0.4 to 1 V progressively suppresses I_D, consistent with the transfer characteristics. In this work, I_{on} and I_{off} are defined as the drain current at $V_{GS} = -0.4$ and 1 V, respectively, with $V_{DS} = -1$ V.

The geometry of organic electrochemical transistors plays a critical role in determining their electrical performance and has been extensively studied. Bernards and Malliaras established the model to depict the relationship between the drain current and the channel dimensions.[3] Based on this model, Rivnay et al. transferred the equations more like a classical field-effect transistor (FET) as shown in eqs 1–3.[26] W and L denote the channel width and length, respectively, and d is the channel thickness. μ represents the charge-carrier mobility of the channel material while C^* is the volumetric capacitance. In interdigitated OECTs, varying the finger geometry effectively modifies W and L, leading to corresponding changes in I_D and g_m.[38] When $V_{DS} \geq V_{GS} - V_T$, the device operates in the saturation regime, and eq 1 reduces to eq 2. Under these conditions, the transconductance in saturation can be obtained by differentiating I_D with respect to V_{GS}, as shown in eq 3.

$$I_D = \frac{Wd}{L}\mu C^*\left(V_T - V_{GS} + \frac{1}{2}V_{DS}\right)V_{DS} \quad (1)$$

$$I_{Dsat} = \frac{Wd}{2L}\mu C^*(V_T - V_{GS})^2 \quad (2)$$

$$g_m = \frac{Wd}{L}\mu C^*(V_T - V_{GS}) \quad (3)$$

Changes in the OECT geometry affect not only the drain current and transconductance but also the threshold voltage. Figure S4a shows the dependence of V_T on the channel thickness. Increasing the spin speed during the spin-coating deposition of the gate material reduces the PEDOT:PSS thickness, where thicker channels exhibit higher V_T. Figure S4b illustrates the effect of the gate area, where increasing the gate area leads to a decrease in V_T. These geometric variations modify the device capacitance, as evidenced by changes in the enclosed area of the cyclic voltammetry curves (Figure S5). Electrochemical impedance spectroscopy (EIS) results also reflect this trend (Figure S6). In general, V_T increases with increasing C_{ch} and decreases with increasing C_g. This behavior can be explained using the OECT equivalent circuit

https://doi.org/10.1021/acsami.6c09414
ACS Appl. Mater. Interfaces XXXX, XXX, XXX–XXX

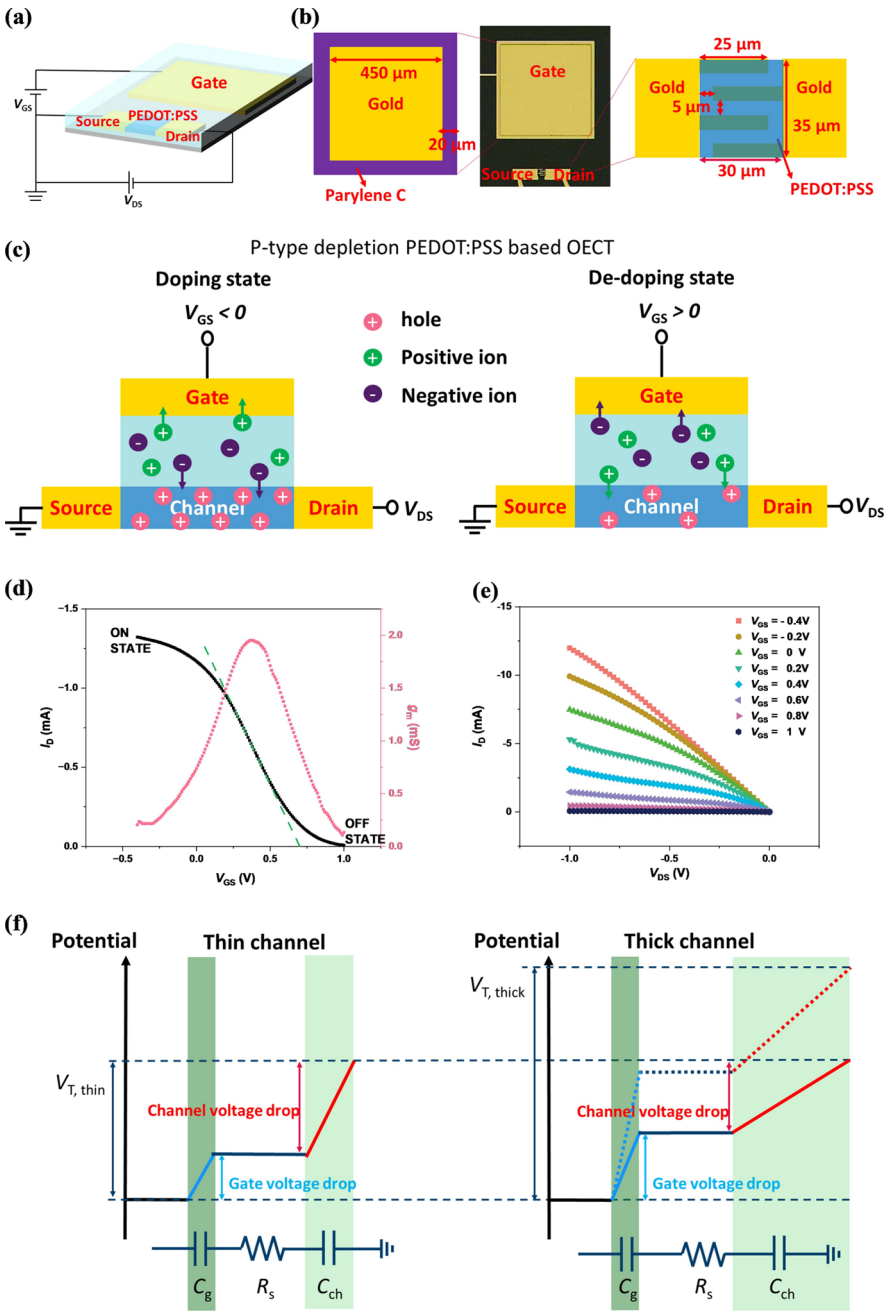

Figure 1. Structural design, working principle, and electrical characterization of the PEDOT:PSS-based OECT. (a) Schematic illustration of the OECT structure. (b) Geometric configuration of the OECT. The central panel displays the actual device layout comprising the gate, source, and drain electrodes. The left panel details the square gate geometry with a side length of 450 μm while the gate edges are passivated with a 20 μm wide PaC layer. The right panel shows the interdigitated transistor channel consisting of four fingers, where the active channel area is built by PEDOT:PSS (blue region). (c) Operating principle: The left schematic illustrates the doped state under negative gate bias ($V_{GS} < 0$), where the hole concentration in the channel is high. The right schematic depicts the dedoped state under positive gate bias ($V_{GS} > 0$), characterized by a reduced hole concentration. (d) Transfer curve of the OECT. The plot displays the transconductance (pink dotted line) and drain current (black dotted line) as functions of V_{GS}. Measurements were performed at a constant V_{DS} of –0.1 V. (e) Output characteristics of the OECT: V_{GS} was swept from –0.4 to 1.0 V in 0.2 V steps, while V_{DS} was scanned from 0 to –1.0 V in –0.02 V steps. The electrical data in (d) and (e) were obtained from an exemplary OECT using 1× PBS as the electrolyte. (f) Equivalent circuit model and potential distribution diagrams to explain the V_T shift mechanism. The model consists of C_g, R_s, and C_{ch}. The diagrams compare the voltage drops across the components for a thin channel (left) versus a thick channel (right). An increase in channel thickness increases C_{ch}, which reduces the voltage drop across the channel and consequently shifts the threshold voltage from $V_{T,\ thin}$ to a higher value, $V_{T,\ thick}$.

https://doi.org/10.1021/acsami.6c09414
ACS Appl. Mater. Interfaces XXXX, XXX, XXX–XXX

(Figure 1f, left), which consists of C_g, the electrolyte resistance R_s, and C_{ch} connected in series.[1,39] C_g corresponds to the electric double-layer capacitance at the gold–electrolyte interface, while C_{ch} represents the volumetric capacitance of the PEDOT:PSS channel, which scales with channel thickness. Upon applying a gate voltage, the voltage is divided between the gate and the channel, with no voltage drop across the electrolyte. The threshold voltage is reached when channel voltage drop V_{ch} induces sufficient channel dedoping, which sets the OECT from the on state to the off state. Increasing the channel thickness increases C_{ch} and reduces V_{ch} for a given V_{GS}. Consequently, a higher V_{GS} is required to reach the threshold, leading to an increased V_T (Figure 1f, right). Similarly, increasing the gate area enhances C_g, increases V_{ch} and reduces V_T. These observations highlight the critical role of the capacitance ratio $C_g/(C_g + C_{ch})$ in governing V_T and its tunability through geometry. This ratio is also known to influence the sensitivity of OECT-based sensors.[30]

However, this capacitance-ratio model alone cannot account for the observed dependence of the threshold voltage on the electrolyte concentration. In our experiments, standard PBS (137 mM NaCl, 2.7 mM KCl, 10 mM Na_2HPO_4 and 1.8 mM KH_2PO_4) was sequentially diluted, yielding electrolyte concentrations of 0.1×, 0.01×, and 0.001× PBS, respectively. As shown in Figure 2a, as the electrolyte concentration decreases, the transfer curves systematically shift toward higher gate voltages, indicating an increase in V_T.

Statistical results from six devices confirm the reproducibility of this trend (Figure 2c). Reducing the electrolyte concentration decreases the ionic strength, which in turn lowers the electrolyte conductivity (Figure 2b, black curve) and modifies the Debye length of the electric double layer (Figure 2b, red curve). These changes alter both the gate capacitance and the channel capacitance, as shown in Figure 2d (C_g in pink, C_{ch} in green). Notably, despite the variations in absolute capacitance values, the ratio $C_g/(C_g + C_{ch})$ remains nearly constant (Figure 2d, purple curve). Consistent with this observation, variations in C_g or C_{ch} alone lead to identical V_T shifts across different electrolyte concentrations (Figure 2e,f), indicating that the capacitance modulation is not the dominant mechanism. In addition, electrolyte resistance emerges as the primary factor governing the V_T shift. This interpretation is supported by the distance-dependent behavior as shown in Figure S7: increasing the separation between the gate and the channel increases the electrolyte resistance, which also results in a systematic increase in V_T.

The influence of the electrolyte concentration extends beyond the V_T modulation. Device-to-device performance variations for six representative devices are presented in Figures S8–S15. As shown in Figure 3a, the absolute value of the on-state current increased only slightly at lower electrolyte concentrations. This behavior can be attributed to suppressed dedoping, as reduced ionic concentration diminishes the ion transport probability across the conductive polymer/electrolyte interface. Simultaneously, the absolute value of the off-state current increased with decreasing electrolyte concentration (Figure 3b), which is a direct consequence of the elevated V_T. A higher V_T requires a larger V_{GS} to fully turn off the channel; thus, at a fixed V_{GS}, the channel remains partially conductive, resulting in higher I_{off}. For example, $V_{GS} = 1$ V is sufficient to fully turn off device 1 at 1× PBS (Figure S8), but not at 0.001× PBS (Figure S11). The on–off ratio (I_{on}/I_{off}) decreased with decreasing electrolyte concentration (Figure 3c), reflecting the fact that I_{off} increases more rapidly than I_{on}. In contrast, the peak g_m remains largely unchanged across electrolyte concentrations (Figure 3d), suggesting that the intrinsic charge-transport properties of the channel are preserved.

Collectively, the observed variations in V_T, I_{on}, I_{off}, and on–off ratio can be explained by electrolyte-induced voltage division. In conventional models (Figure 3e), the applied V_{GS} is assumed to drop exclusively across the gate/electrolyte interface and the channel. However, at low electrolyte concentrations, the electrolyte resistance becomes non-negligible and contributes significantly to the voltage drop. This electrolyte-induced voltage division is further supported by the experimentally observed distance-dependent V_T shifts (Figure S7). This voltage-division mechanism is also supported by recent literature on solid-state OECTs, where thermally tuned electrolyte resistance similarly drives systematic shifts in the threshold voltage.[35]

Incorporating Ohm's law into the voltage-division model introduces an additional resistive term, yielding the channel voltage drop V_{ch} as expressed in eq 4. Here, C_g and C_{ch} denote the gate and channel capacitances, respectively. R_s is the electrolyte resistance between the gate and channel, j is the imaginary unit, and ω is the angular frequency ($\omega = 2\pi f$, where f is the frequency).

$$V_{ch} = \frac{\frac{1}{j\omega C_{ch}}}{\frac{1}{j\omega C_{ch}} + \frac{1}{j\omega C_g} + R_s} V_{GS} \tag{4}$$

By taking the magnitude of the complex voltage drop, we can obtain eq 5

$$|V_{ch}| = \frac{C_g}{\sqrt{(C_g + C_{ch})^2 + C_g^2 C_{ch}^2 R_s^2 \omega^2}} V_{GS} \tag{5}$$

where $|V_{ch}|$ is the effective voltage drop across the channel. Although $|V_{ch}|$ is challenging to probe directly through experimental means, its dynamic variations can be inferred through shifts in the threshold voltage. Specifically, the threshold voltage can be considered as the V_{GS} at which the channel transitions from the on state to the off state, corresponding to a change from the doped to the dedoped regime. At this condition, the magnitude of the channel voltage reaches a critical value, denoted as V_{ch}', which is the voltage sufficient to fully turn off the channel. By substituting V_{GS} with V_T and $|V_{ch}|$ with V_{ch}' in the voltage-division expression, the resulting relationship between V_T, the gate and channel capacitances, and the electrolyte resistance is obtained, as given in eq 6.

$$V_T = V_{ch}' \frac{\sqrt{(C_g + C_{ch})^2 + C_g^2 C_{ch}^2 R_s^2 \omega^2}}{C_g} \tag{6}$$

This impedance-based relationship not only accounts for the influence of gate and channel capacitances on the threshold voltage but also explains why both electrolyte concentration and the gate–channel separation significantly affect OECT operation. By explicitly incorporating electrolyte resistance, the voltage-division model can be revised as illustrated in Figure 3e. In contrast to the conventional capacitive model (Figure 3e, left), the impedance-based framework (Figure 3e,

https://doi.org/10.1021/acsami.6c09414
ACS Appl. Mater. Interfaces XXXX, XXX, XXX–XXX

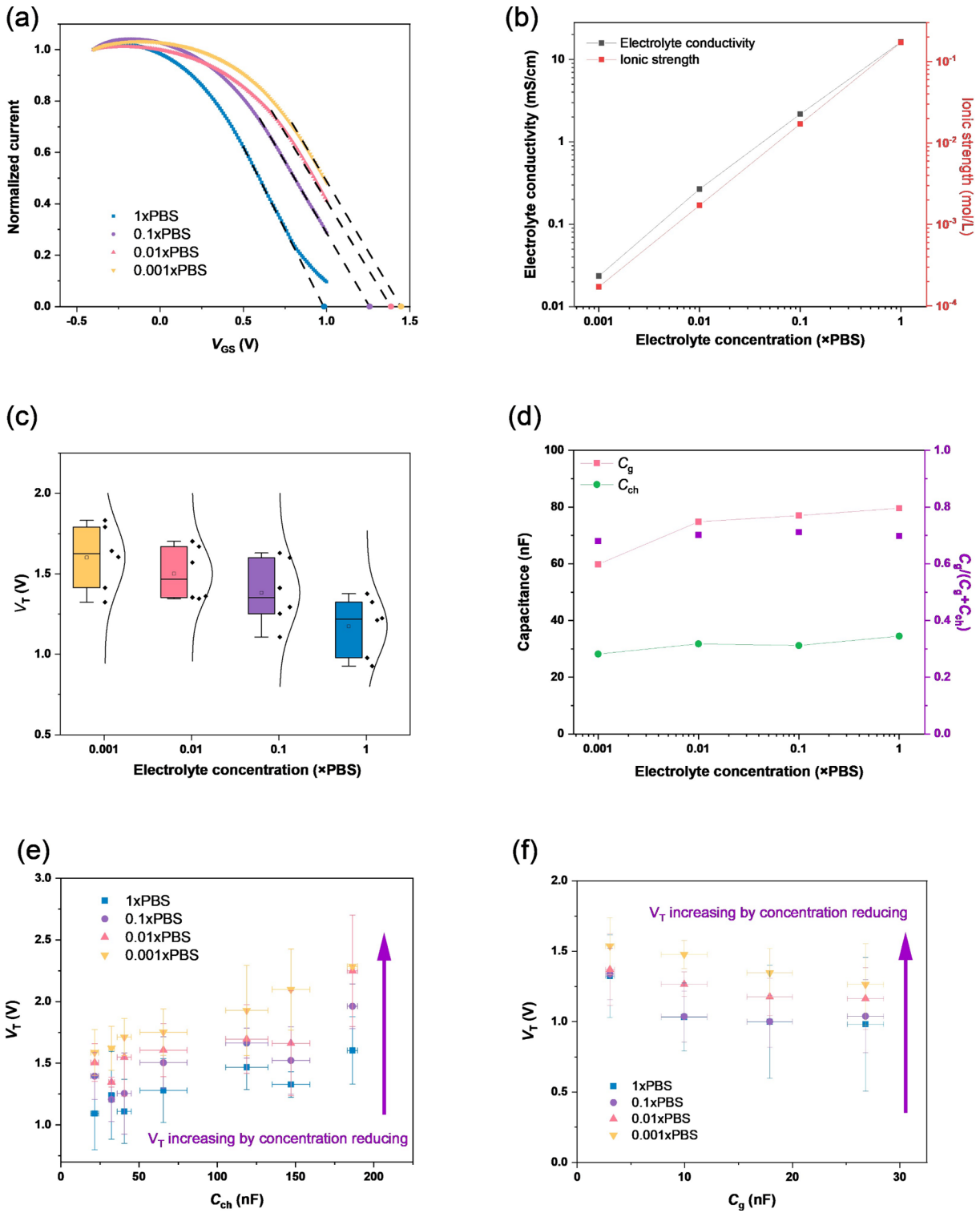

Figure 2. Influence of the electrolyte concentration on the OECT performance and capacitance. (a) Normalized transfer curves ($I_D/I_{D,\,ref}$–V_{GS}) for OECTs measured in PBS electrolytes of varying concentrations (1×, 0.1×, 0.01×, and 0.001×). The reference current, $I_{D,\,ref}$, is I_D at $V_{GS} = -0.4$ V. Black dashed lines represent the tangents used to extract the V_T. (b) Electrolyte conductivity (black, measured) and ionic strength (red, calculated) as a function of PBS concentration. Both parameters increase with higher electrolyte concentration. (c) V_T as a function of electrolyte concentration. The box plots show the statistical distribution of V_T values, which systematically decreases with increasing electrolyte concentration. Individual data points are overlaid as black dots. (d) C_g (purple) and C_{ch}, (green), along with the ratio $C_g/(C_g + C_{ch})$ (right y-axis), plotted against electrolyte concentration. C_g and C_{ch} show a dependence on concentration, while their ratio remains relatively constant. (e, f) V_T plotted against C_g in (e) and C_{ch} in (f), with data color-coded by electrolyte concentration. These plots decouple the effects of C_g and C_{ch} on V_T. Data in (e) are from $n = 28$ devices, and data in (f) are from $n = 14$ devices. All measurements were performed with a constant $V_{DS} = -0.1$ V. The devices featured a 450 μm square gate and a 30 μm × 35 μm channel. All the capacitance data are extracted by EIS fitting based on the circuit shown in Figure S6a.

https://doi.org/10.1021/acsami.6c09414
ACS Appl. Mater. Interfaces XXXX, XXX, XXX–XXX

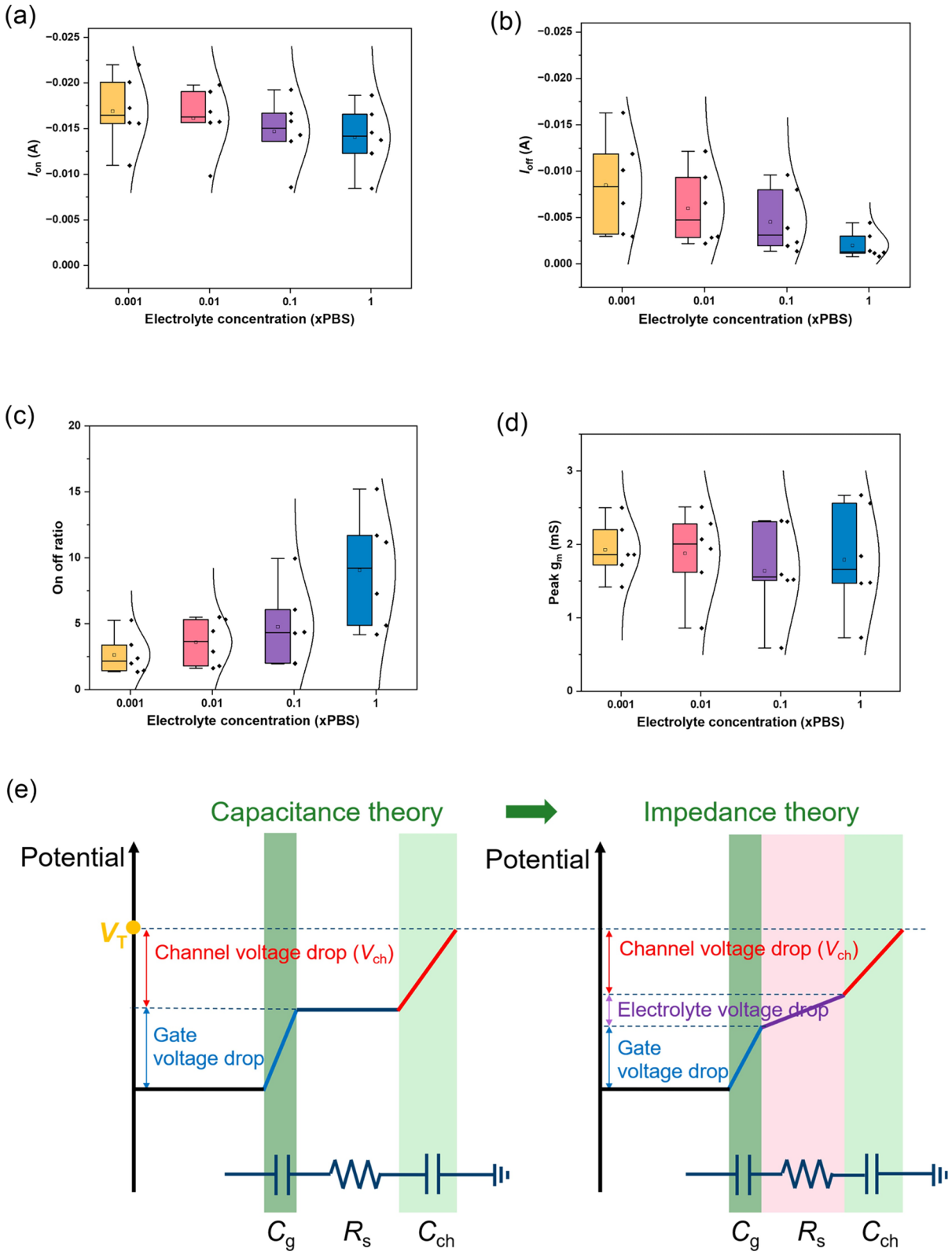

Figure 3. Impact of the electrolyte concentration on the OECT characteristics and introduction of a revised impedance model. (a–d) Statistical distribution of key OECT performance metrics as a function of electrolyte concentration: (a) on-state current, (b) off-state current, (c) on–off ratio, and (d) peak g_m. The box plots illustrate the data distribution, with individual measurements overlaid as black dots. (e) Comparison of equivalent circuit models for potential distribution in an OECT. The classical "Capacitance theory" (left) considers voltage drops only across the C_g and C_{ch}. The newly proposed "Impedance theory" (right) incorporates the R_s, which introduces an additional voltage drop ("electrolyte voltage drop"). Data in (a–d) were collected from OECTs with a 450 μm square gate and a 30 μm × 35 μm channel, featuring a channel capacitance in the range of 18.9–26 nF. All measurements were performed at a constant V_{DS} = –0.1 V.

https://doi.org/10.1021/acsami.6c09414
ACS Appl. Mater. Interfaces XXXX, XXX, XXX–XXX

right) introduces an additional voltage drop across the electrolyte. The magnitude of this electrolyte-induced voltage division can be quantitatively determined from the impedance ratio of the gate, channel, and electrolyte. This impedance model has the potential to be applied to other material systems. For channel materials, other OMIECs, such as poly(benzimidazobenzophenanthroline) (BBL),[40] can also follow this model because these OMIECs operate based on volumetric ion injection and volumetric capacitance. Therefore, their characteristic performance scaling can be represented in a similar manner to PEDOT:PSS. Regarding the electrolytes, our model can be utilized in other water-based solutions where the mobile ions act as an electrolyte resistance. It is worth noting that the present impedance-based framework established here represents a foundational baseline model for pristine OECTs. However, when specific surface modifications are implemented, additional circuit elements must be integrated to capture the reconfigured system behavior. For instance, incorporating an ion-selective membrane (ISM) on the gate introduces an extra phase-boundary potential,[41] whereby the gate voltage drop and the equivalent circuit model must be thoroughly re-evaluated.

Furthermore, the transconductance, defined as the derivative of the transfer characteristic (Eq 3), also shifts along the V_{GS} axis, thereby displacing the operation point corresponding to peak g_m. To experimentally investigate the frequency dependence, an alternating gate bias was applied, as schematically shown in Figure 4a. The applied V_{GS} consists of a DC bias component (V_{bias}) superimposed with a sinusoidal AC signal of fixed amplitude (50 mV) and a variable frequency f. The V_{DS} was held constant at −0.1 V.

As illustrated in Figure 4c, the sinusoidal modulation of V_{GS} (top panel) induces a corresponding periodic response in the I_D (middle panel). The peak and valley values of I_D were extracted over time, and the current modulation amplitude was calculated as $(I_{peak}–I_{valley})/2$. Dividing this value by the AC gate-voltage amplitude (50 mV) yields the real-time transconductance (dynamic transconductance), denoted as $g_{m,r}$ (Figure 4c, bottom panel). The extracted $g_{m,r}$ is initially time dependent and influenced by V_{GS}, as shown in Figure S16. Therefore, in this study, a steady-state $g_{m,r}$ was defined as the time-averaged value over the final 20 periods, during which $g_{m,r}$ stabilizes.

Importantly, our proposed impedance model predicts that V_T is also frequency dependent. An increase in V_T leads to a rightward shift of the transfer curve, as described by Figure S4a,b.

By sweeping V_{bias} at a fixed frequency ($f = 1$ Hz), the $g_{m,r}$ vs V_{bias} relationship as shown in Figure 4b was obtained. The green data points represent $g_{m,r}$ extracted from the AC measurements at different V_{bias} values, while the pink points correspond to g_m values derived from the DC transfer curve, where V_{GS} contains only a static component. Both datasets exhibit the same characteristic behavior: g_m increases with V_{bias}, reaches a maximum at the operation point, and then decreases at higher V_{bias}, confirming the consistency between AC and DC transconductance analyses. However, it is worth noting that while their overall trends are consistent, the static g_m remains systematically higher than the dynamic $g_{m,r}$. Microscopically, this discrepancy stems from the fact that static g_m reflects a fully equilibrated, steady-state electrochemical doping process under static DC biases. In contrast, the dynamic charge transduction under AC modulation is fundamentally bound by the finite kinetic relaxation of ion motion into and out of the polymer bulk, which renders the transient current modulation less efficient than its steady-state counterpart. Developing an advanced dynamic transconductance model that integrates these transient ion-transport parameters represents a critical and promising direction for our future investigations. Macroscopically, this discrepancy inherently reflects the fundamental performance distinction between static and dynamic operating regimes. Subsequently, the frequency of the AC gate modulation was increased from $f = 1$ to 100 Hz, and the resulting $g_{m,r}$ vs V_{bias} curves at different frequencies are shown in Figure 4d. Although the overall shape of the curves remains similar across frequencies, the peak $g_{m,r}$ systematically decreases as the frequency increases, consistent with previous reports that higher-frequency inputs reduce the amplification capability of OECTs.[42] Notably, this frequency-dependent attenuation occurs across the entire V_{bias} range.

More importantly, increasing the frequency induces a pronounced shift in the operation point of the $g_{m,r}$–V_{bias} curve. For example, the V_{bias} corresponding to peak $g_{m,r}$ shifts from 0.4 V at $f = 1$ Hz to 0.6 V at $f = 5$ Hz (Figure 4d). This behavior is consistent with eq 6, which predicts a frequency-induced rightward shift in V_T. Physically, an elevated operating frequency diminishes the capacitive impedance of the system, causing R_s to consume a larger share of the voltage drop. Consequently, the effective voltage drop across the channel $|V_{ch}|$ is significantly reduced, meaning that a higher external potential is required to achieve the critical channel potential for depletion, which manifests macroscopically as the rightward drift of V_T. As V_T increases, a higher gate bias is required to reach the optimal transconductance regime. Furthermore, eq 6 indicates that modifying the relative contributions of C_g and C_{ch} leads to different operation points. This effect is experimentally confirmed in Figure 4d,e, which show the influence of gate area on $g_{m,r}$. Devices with larger gate areas require lower V_{bias} to reach peak $g_{m,r}$, whereas higher input frequencies consistently demand higher V_{bias} to recover optimal amplification.

Leveraging this frequency-dependent operation-point shift, we propose a new operation point tuning strategy as a simple yet effective method to enhance the high-frequency amplification performance of OECTs. For instance, as shown in Figure 4d, when a 5 Hz signal is applied, $g_{m,r}$ is 0.77 mS at $V_{bias} = 0.4$ V; increasing V_{bias} to 0.6 V enhances $g_{m,r}$ by approximately 12% to 0.86 mS. Similarly, at $f = 50$ Hz, adjusting V_{bias} from 0.4 to 0.6 V yields an 18.0% increase in $g_{m,r}$. To the best of our knowledge, this is the first demonstration of improving the high-frequency performance of OECTs solely through electrical bias optimization. Comparing with traditional OECT optimization methods, which concentrate on channel material design strategies,[43–45] geometrical optimization,[38,46] or new structure design,[47,48] our proposed operation point tuning strategy is very convenient and powerful. This approach provides a powerful and practical pathway to further unlock the potential of OECTs for high-speed and high-sensitivity electrical sensing applications.

3. CONCLUSION

In this work, we investigated the influence of device geometry and channel thickness on the electrical characteristics of organic electrochemical transistors. Variations in these parameters induce shifts in the threshold voltage, which can be

https://doi.org/10.1021/acsami.6c09414
ACS Appl. Mater. Interfaces XXXX, XXX, XXX–XXX

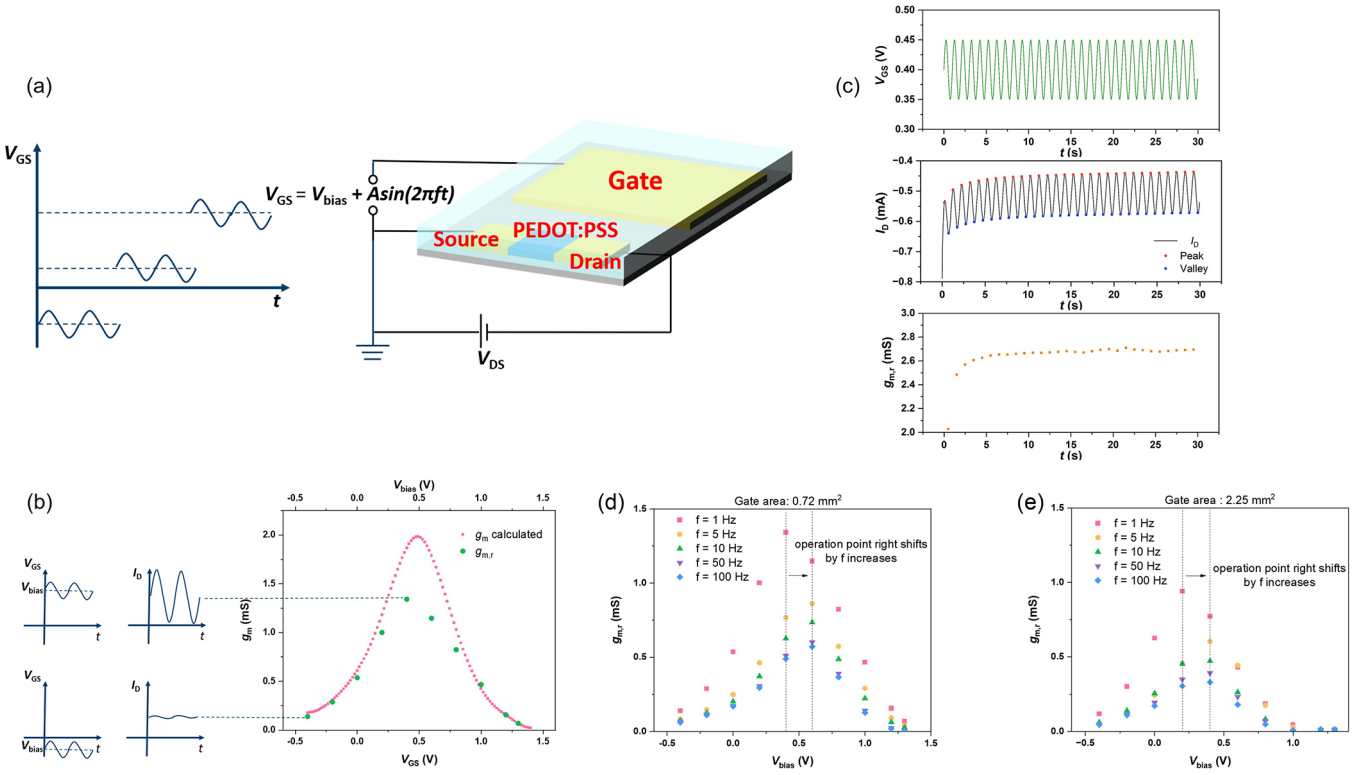

Figure 4. Dynamic response of OECTs to sinusoidal gate voltage modulation and frequency-dependent transconductance: (a) Schematic illustrating the experimental setup and applied waveforms. A DC bias (V_{DS} = –0.1 V) is applied to the drain, while a combined DC and AC sinusoidal voltage ($V_{GS} = V_{bias} + A\sin(2\pi ft)$) is applied to the gate. (b) Analysis of the device's transconductance: the four plots on the left show the I_D response to a small sinusoidal V_{GS} at different DC bias points (V_{bias}). The amplitude of the I_D response is larger when V_{bias} is near the peak g_m and decreases as V_{bias} moves away from the peak. The plot on the right compares two methods of extracting g_m: the static transconductance (g_m, pink), calculated by differentiating the DC transfer curve, and the dynamic transconductance ($g_{m,r}$, green), calculated from the ratio of the AC current and voltage amplitudes under sinusoidal modulation. While both show a similar trend of increasing and then decreasing, the static g_m is consistently higher than the dynamic $g_{m,r}$. (c) Time-resolved electrical response of an OECT under continuous sinusoidal gate modulation. Top: Applied V_{GS}. Middle: Resulting I_D, showing distinct peak and valley values within each cycle. Bottom: Calculated instantaneous dynamic transconductance $g_{m,r}$ over time, demonstrating stable operation. (d, e) $g_{m,r}$ as a function of V_{bias} for devices with different gate areas at various modulation frequencies (1–100 Hz): (d) 0.72 and (e) 2.25 mm^2. Two key trends are observed: (1) at a fixed V_{bias}, $g_{m,r}$ decreases with increasing frequency. (2) The V_{bias} position corresponding to the peak $g_{m,r}$ shifts to higher voltages (rightward shift) as the frequency increases. Specifically, in (d), the peak shifts from 0.4 (1 Hz) to 0.6 V (5 Hz); in (e), it shifts from 0.2 to 0.4 V. This frequency-dependent shift varies with gate area. All measurements were performed with a constant V_{DS} = –0.1 V and a fixed AC amplitude. The channel dimensions were 30 μm × 35 μm for all devices.

rationalized within the conventional capacitance-ratio framework through corresponding changes in the relative gate and channel capacitances. However, this model alone fails to account for the pronounced performance variations observed at fixed capacitance ratios when the electrolyte concentration or the gate–channel distance are altered. To address this limitation, we extend the capacitance-ratio model to an impedance-based framework in which the electrolyte resistance plays a non-negligible role in the voltage division. Within this impedance theory, the electrolyte contributes an additional voltage drop comparable to those across the gate and along the channel, providing a unified explanation for the effects of electrolyte concentration and gate–channel separation on OECT performance.

Beyond static bias conditions, the impedance model further predicts a frequency-dependent modulation of device operation. Specifically, increasing the signal frequency input induces a rightward shift of the transfer characteristics, the g_m–V_{GS} curve, and the corresponding operation point. This prediction is successfully validated through AC gate-bias measurements, which reveal that higher-frequency signals require a larger V_{bias} to achieve their peak dynamic transconductance values. These results confirm that the commonly observed degradation in amplification capability at higher frequencies can be partially attributed to frequency-induced shifts in V_T, rather than solely to intrinsic transport limitations.

Importantly, this insight enables a practical and previously unexplored strategy for enhancing high-frequency OECT performance: dynamic tuning of V_{GS}, or equivalently its DC component V_{bias}, to compensate for frequency-dependent operation-point shifts. This approach improves amplification without modifying device geometry, materials, or fabrication processes. While this strategy does not bypass the intrinsic material-defined bandwidth limitations of OECTs under ultra-high-frequency regimes, it effectively extends their operational frequency range as a convenient engineering solution. Generally, the impedance-based framework and operation point tuning strategy introduced here provide a universal methodology for optimizing OECTs and other electrolyte-gated devices in frequency-sensitive applications, thereby

https://doi.org/10.1021/acsami.6c09414
ACS Appl. Mater. Interfaces XXXX, XXX, XXX–XXX

expanding their potential in high-speed bioelectronics and electrical sensing technologies.

4. EXPERIMENTAL SECTION

Device Fabrication

OECTs were fabricated on 4 inch quartz glass wafers. The detailed process flow is shown in Figure S17. Before the actual processing, the wafers were washed with acetone, isopropanol, and water to clean the substrate surface. Then a PaC layer with a thickness of 5 μm was deposited using a PDS 2010 Labcoater 2 (Specialty Coating Systems Inc., USA). To achieve an ideal undercut profile and improve the yield and reliability of the lift-off process, a bilayer photoresist strategy was employed. The photoresist LOR3B (Microchem, Newton, USA) was spin coated (4 mL, 3000 rpm, 30 s) on the surface. After soft baking the LOR3B for 5 min at 150 °C, 4 mL of nLOF2020 (MicroChemicals, Ulm, Germany) was spin coated (3000 rpm, 30 s), followed by another soft baking step (110 °C, 1 min). For the exposure of the photoresist, a maskless aligner (MLA 150, Heidelberg Instruments Mikrotechnik GmbH, Heidelberg, Germany) was used with a dose of 350 mJ/cm^2. After a post exposure bake (110 °C, 2 min) on a hot plate, devices were developed for 33–35 s in the developer AZ 326 MIF (MicroChemicals, Ulm, Germany). Then, the metal film consisting of 20 nm Ti as adhesion promoter and 100 nm Au was deposited by an electron-beam evaporation system (Pfeiffer PLS 570, Pfeiffer Vacuum, Asslar, Germany) after a 90 s Ar dry etching to remove resist residuals. DMSO was chosen as the solvent for an overnight lift-off. Afterward, the wafers were partially diced to support later the separation of the wafer into individual chips. Then another PaC layer with a thickness of 5 μm was deposited as passivation layer. To etch the covering PaC layer on the OECT terminals, another photolithography step was done using AZ 12XT (MicroChemicals, Ulm, Germany) as resist and utilizing the same MLA machine with a dose of 270 mJ/cm^2. The soft bake was done at 110 °C for 2 min and the post exposure bake was done at 90 °C for 1 min. The wafers were then developed in AZ 326 MIF developer for 5 min. Reactive ion etching was done using a mixture of CF_4 and O_2 in an Oxford PL100 system (Oxford Instruments, UK) for 7 min 30 s. Extra resist was removed by DMSO. To pattern the PEDOT:PSS, another photolithography process was performed utilizing again the photoresist AZ 12XT with the same condition as mentioned above. After development, the wafer surface was activated by an oxygen plasma (Diener electronics GmbH, Ebhausen, Germany) under 100% power, 0.8 mbar O_2 for 10 min to increase the adhesion of the PEDOT:PSS film. A Clevios PH-1000 PEDOT:PSS solution (Heraeus Holding GmbH, Germany) was filtered using a syringe filter with a pore size of 0.8 μm. 10% (v/v) DMSO and 1% (v/v) GOPS (Sigma-Aldrich) were used as additives. This solution was spin coated at 4000 rpm for 90 s by a WS-650Lz spin-coater (Laurell Technologies, USA). After baking the chip at 120 °C for 20 min, DMSO was used to lift off the extra PEDOT:PSS. Then, the wafer was broken along the predicted trenches into pieces. Subsequently, home-made glass rings were glued onto the central area of each chip to be used as liquid cell. The chips were electrically connected through a socket with spring contacts (Yamaichi Electronics Deutschland GmbH, Germany) to facilitate a parallel characterization of multiple devices. All above chemicals were obtained from Sigma (Sigma-Aldrich, Steinheim, Germany) and used without further purification.

Electrical Characterization

The transfer curves and output curves were measured using a parameter-analyzer Keithley 4200. For the transfer characteristics, V_{DS} was set to –0.1 V, while V_{GS} was swept. For the output characteristics, V_{DS} was scanned from 0 to -1 V, while V_{GS} was set to values between –0.4 and 1 V. The data were then recorded and processed by Origin software.

Electrochemical Characterization

Cyclic voltammetry measurements were recorded by an Autolab potentiostat/galvanostat PGSTAT302 (Metrohm Autolab, Netherlands). A three-electrode configuration was used, which comprised an Ag/AgCl electrode as reference, a platinum wire as counter electrode, and the OECT terminal (channel or gate) as a working electrode. The electrolyte was a standard phosphate buffered saline (1× PBS pH 7.4). The scan range of the working electrode was from –0.7 to 0.7 V.

Electrochemical impedance spectroscopy was done by the same potentiostat with a three-electrode configuration system. The frequency was scanned in the range from 0.1 Hz to 10^5 Hz. The amplitude of this alternating voltage was 0.01 V_{RMS}.

Frequency Characterization

All the OECT characterizations with alternating V_{GS} at varying frequency were performed with an Arkeo parameter analyzer (Arkeo, Cicci Research, Italy), which has two independent source measure units (SMU). One SMU was used to apply a fixed –0.1 V direct voltage as V_{DS}. Another SMU applied a sine wave (A = 50 mV, f = 1, 5, 10, 50, and 100) with various V_{bias} as alternating V_{GS}. A fixed sample resolution of 20 points per period was chosen. After collecting 30 periods for each device, the data were analyzed by a Python code.

■ ASSOCIATED CONTENT

Data Availability Statement

The data that support the findings of this study are available from the corresponding author upon reasonable request.

Supporting Information

The Supporting Information is available free of charge at https://pubs.acs.org/doi/10.1021/acsami.6c09414.

OECT measurement setup (Figure S1); structure and dedoping principle of PEDOT:PSS (Figure S2); method for the extraction of V_T from the transfer characteristics of the OECTs (Figure S3); transfer characteristics of OECTs with varying structural parameters (Figure S4); cyclic voltammetry curves of OECTs under varying structural parameters (Figure S5); electrochemical impedance spectroscopy characterization (Figure S6); transfer characteristics of OECTs with varying gate-channel distances (Figure S7); output curves of six devices in four various concentration electrolyte (Figures S8–S11); transfer and g_m–V_{GS} curves of six devices in four various concentration electrolyte (Figures S12–S15); $g_{m,r}$–t curve with various V_{bias} (Figure S16); complete process flow for OECT fabrication (Figure S17) (DOCX)

■ AUTHOR INFORMATION

Corresponding Author

Dirk Mayer – *Institute of Biological Information Processing, Bioelectronics IBI-3, Forschungszentrum Jülich, Jülich 52425, Germany*; orcid.org/0000-0003-1296-8265; Email: dirk.mayer@fz-juelich.de

Authors

Qinyu Hu – *Institute of Biological Information Processing, Bioelectronics IBI-3, Forschungszentrum Jülich, Jülich 52425, Germany; Institute of Materials in Electrical Engineering 1, RWTH Aachen University, Aachen 52074, Germany*; orcid.org/0000-0002-1839-1551

https://doi.org/10.1021/acsami.6c09414
ACS Appl. Mater. Interfaces XXXX, XXX, XXX–XXX

Hangyu Li – *Institute of Biological Information Processing, Bioelectronics IBI-3, Forschungszentrum Jülich, Jülich 52425, Germany*
Shengkai Sun – *Institute of Biological Information Processing, Bioelectronics IBI-3, Forschungszentrum Jülich, Jülich 52425, Germany*
Viviana Rincón Montes – *Institute of Biological Information Processing, Bioelectronics IBI-3, Forschungszentrum Jülich, Jülich 52425, Germany*
Sven Ingebrandt – *Institute of Materials in Electrical Engineering 1, RWTH Aachen University, Aachen 52074, Germany*; orcid.org/0000-0002-0405-2727
Francesca Santoro – *Institute of Biological Information Processing, Bioelectronics IBI-3, Forschungszentrum Jülich, Jülich 52425, Germany; Neuroelectronic Interfaces, Faculty of Electrical Engineering and IT, RWTH Aachen University, Aachen 52074, Germany*; orcid.org/0000-0001-7323-9504
Andreas Offenhäusser – *Institute of Biological Information Processing, Bioelectronics IBI-3, Forschungszentrum Jülich, Jülich 52425, Germany*; orcid.org/0000-0001-6143-2702

Complete contact information is available at: https://pubs.acs.org/doi/10.1021/acsami.6c09414

Notes

The authors declare no competing financial interest.

■ ACKNOWLEDGMENTS

The device was fabricated in the Helmholtz Nano Facility of Forschungszentrum Jülich GmbH, and we thank the technicians and engineers for their assistance. Q.H. gratefully appreciates the financial support from the China Scholarship Council (202104910077).

■ REFERENCES

(1) Rivnay, J.; Inal, S.; Salleo, A.; Owens, R. M.; Berggren, M.; Malliaras, G. G. Organic Electrochemical Transistors. *Nat. Rev. Mater.* **2018**, *3* (2), No. 17086.
(2) Kukhta, N. A.; Marks, A.; Luscombe, C. K. Molecular Design Strategies toward Improvement of Charge Injection and Ionic Conduction in Organic Mixed Ionic–Electronic Conductors for Organic Electrochemical Transistors. *Chem. Rev.* **2022**, *122* (4), 4325–4355.
(3) Bernards, D. A.; Malliaras, G. G. Steady-State and Transient Behavior of Organic Electrochemical Transistors. *Adv. Funct. Mater.* **2007**, *17* (17), 3538–3544.
(4) Inal, S.; Rivnay, J.; Leleux, P.; Ferro, M.; Ramuz, M.; Brendel, J. C.; Schmidt, M. M.; Thelakkat, M.; Malliaras, G. G. A High Transconductance Accumulation Mode Electrochemical Transistor. *Adv. Mater.* **2014**, *26* (44), 7450–7455.
(5) Khodagholy, D.; Rivnay, J.; Sessolo, M.; Gurfinkel, M.; Leleux, P.; Jimison, L. H.; Stavrinidou, E.; Herve, T.; Sanaur, S.; Owens, R. M.; Malliaras, G. G. High Transconductance Organic Electrochemical Transistors. *Nat. Commun.* **2013**, *4* (1), No. 2133.
(6) Wang, L.; Sun, Q.; Zhang, L.; Wang, J.; Ren, G.; Yu, L.; Wang, K.; Zhu, Y.; Lu, G.; Yu, H.-D. Realizing Ultrahigh Transconductance in Organic Electrochemical Transistor by Co-Doping PEDOT:PSS with Ionic Liquid and Dodecylbenzenesulfonate. *Macromol. Rapid Commun.* **2022**, *43* (17), No. 2200212.
(7) Yao, Y.; Huang, W.; Chen, J.; Liu, X.; Bai, L.; Chen, W.; Cheng, Y.; Ping, J.; Marks, T. J.; Facchetti, A. Flexible and Stretchable Organic Electrochemical Transistors for Physiological Sensing Devices. *Adv. Mater.* **2023**, *35* (35), No. 2209906.
(8) Nawaz, A.; Liu, Q.; Leong, W. L.; Fairfull-Smith, K. E.; Sonar, P. Organic Electrochemical Transistors for In Vivo Bioelectronics. *Adv. Mater.* **2021**, *33* (49), No. 2101874.
(9) Stříteský, S.; Marková, A.; Víteček, J.; Šafaříková, E.; Hrabal, M.; Kubáč, L.; Kubala, L.; Weiter, M.; Vala, M. Printing Inks of Electroactive Polymer PEDOT:PSS: The Study of Biocompatibility, Stability, and Electrical Properties. *J. Biomed. Mater. Res., Part A* **2018**, *106* (4), 1121–1128.
(10) Mangoma, T. N.; Yamamoto, S.; Malliaras, G. G.; Daly, R. Hybrid 3D/Inkjet-Printed Organic Neuromorphic Transistors. *Adv. Mater. Technol.* **2022**, *7* (2), No. 2000798.
(11) Afonso, M.; Morgado, J.; Alcácer, L. Inkjet Printed Organic Electrochemical Transistors with Highly Conducting Polymer Electrolytes. *J. Appl. Phys.* **2016**, *120* (16), No. 165502.
(12) Khoury, F.; Saleh, S.; Badawe, H.; Obeid, M.; Khraiche, M. Inkjet-Printed, Flexible Organic Electrochemical Transistors for High-Performance Electrocorticography Recordings. *ACS Appl. Mater. Interfaces* **2024**, *16* (41), 55045–55055.
(13) Zabihipour, M.; Janson, P.; Berggren, M.; Simon, D. T.; Andersson Ersman, P.; Engquist, I. Organic Electrochemical Transistors Manufactured by Laser Ablation and Screen Printing. *Flex. Print. Electron.* **2022**, *7* (3), No. 035018.
(14) Rashid, R. B.; Ciechowski, R. J.; Rivnay, J. Self-Aligned, Laser-Cut Organic Electrochemical Transistors. *Flex. Print. Electron.* **2020**, *5* (1), No. 014007.
(15) Tran, V. C.; Mastantuoni, G. G.; Zabihipour, M.; Li, L.; Berglund, L.; Berggren, M.; Zhou, Q.; Engquist, I. Electrical Current Modulation in Wood Electrochemical Transistor. *Proc. Natl. Acad. Sci.* **2023**, *120* (18), No. e2218380120.
(16) Spyropoulos, G. D.; Gelinas, J. N.; Khodagholy, D. Internal ion-gated organic electrochemical transistor: A building block for integrated bioelectronics. *Sci. Adv.* **2019**, *5*, (2), No. eaau7378.
(17) Cea, C.; Spyropoulos, G. D.; Jastrzebska-Perfect, P.; Ferrero, J. J.; Gelinas, J. N.; Khodagholy, D. Enhancement-Mode Ion-Based Transistor as a Comprehensive Interface and Real-Time Processing Unit for in Vivo Electrophysiology. *Nat. Mater.* **2020**, *19* (6), 679–686.
(18) Liu, H.; Song, J.; Zhao, Z.; Zhao, S.; Tian, Z.; Yan, F. Organic Electrochemical Transistors for Biomarker Detections. *Adv. Sci.* **2024**, *11* (27), No. 2305347.
(19) Xi, X.; Wu, D.; Ji, W.; Zhang, S.; Tang, W.; Su, Y.; Guo, X.; Liu, R. Manipulating the Sensitivity and Selectivity of OECT-Based Biosensors via the Surface Engineering of Carbon Cloth Gate Electrodes. *Adv. Funct. Mater.* **2020**, *30* (4), No. 1905361.
(20) Kim, J.; Pankow, R. M.; Cho, Y.; Duplessis, I. D.; Qin, F.; Meli, D.; Daso, R.; Zheng, D.; Huang, W.; Rivnay, J.; Marks, T. J.; Facchetti, A. Monolithically Integrated High-Density Vertical Organic Electrochemical Transistor Arrays and Complementary Circuits. *Nat. Electron.* **2024**, *7* (3), 234–243.
(21) Andersson Ersman, P.; Lassnig, R.; Strandberg, J.; Tu, D.; Keshmiri, V.; Forchheimer, R.; Fabiano, S.; Gustafsson, G.; Berggren, M. All-Printed Large-Scale Integrated Circuits Based on Organic Electrochemical Transistors. *Nat. Commun.* **2019**, *10* (1), No. 5053.
(22) Ji, J.; Wang, H.; Liu, R.; Jiang, X.; Zhang, Q.; Peng, Y.; Sang, S.; Sun, Q.; Wang, Z. L. Dual-Liquid-Gated Electrochemical Transistor and Its Neuromorphic Behaviors. *Nano Energy* **2021**, *87*, No. 106116.
(23) Yamamoto, S.; Polyravas, A. G.; Han, S.; Malliaras, G. G. Correlation between Transient Response and Neuromorphic Behavior in Organic Electrochemical Transistors. *Adv. Electron. Mater.* **2022**, *8* (4), No. 2101186.
(24) van de Burgt, Y.; Lubberman, E.; Fuller, E. J.; Keene, S. T.; Faria, G. C.; Agarwal, S.; Marinella, M. J.; Alec Talin, A.; Salleo, A. A Non-Volatile Organic Electrochemical Device as a Low-Voltage Artificial Synapse for Neuromorphic Computing. *Nature Mater.* **2017**, *16* (4), 414–418.
(25) Pecunia, V.; Petti, L.; Andrews, J. B.; Ollearo, R.; Gelinck, G. H.; Nasrollahi, B.; Jailani, J. M.; Li, N.; Kim, J. H.; Ng, T. N.; Feng, H.; Chen, Z.; Guo, Y.; Shen, L.; Lhuillier, E.; Kuo, L.; Sangwan, V. K.; Hersam, M. C.; Fraboni, B.; Basiricò, L.; Ciavatti, A.; Wu, H.; Niu, G.; Tang, J.; Yang, G.; Kim, D.; Dremann, D.; Jurchescu, O. D.; Bederak,

D.; Shulga, A. G.; Costa, P.; Perinka, N.; Lanceros-Mendez, S.; Chortos, A.; Khuje, S.; Yu, J.; Ren, S.; Mascia, A.; Concas, M.; Cosseddu, P.; Young, R. J.; Yokota, T.; Somoya, T.; Jeon, S. J.; Zhao, N.; Li, Y.; Shukla, D.; Wu, S.; Zhu, Y.; Takei, K.; Huang, Y.; Spiece, J.; Gehring, P.; Persaud, K.; Llobet, E.; Krik, S.; Vasquez, S.; Costa Angeli, M. A.; Lugli, P.; Fabbri, B.; Spagnoli, E.; Rossi, A.; Occhipinti, L. G.; Tang, C.; Yi, W.; Ravenscroft, D.; Kandukuri, T. R.; Abideen, Z. U.; Azimi, Z.; Tricoli, A.; Rivadeneyra, A.; Rojas, S.; Gaiardo, A.; Valt, M.; Galstyan, V.; Zappa, D.; Comini, E.; Noël, V.; Mattana, G.; Piro, B.; Strand, E.; Bihar, E.; Whiting, G. L.; Shkodra, B.; Petrelli, M.; Moro, G.; Raucci, A.; Miglione, A.; Cinti, S.; Casson, A. J.; Wang, Z.; Bird, D.; Batchelor, J. C.; Xing, L.; Johnson, L. S. J.; Alwattar, A. A.; Kyndiah, A.; Viola, F. A.; Caironi, M.; Albarghouthi, F. M.; Smith, B. N.; Franklin, A. D.; Pal, A.; Banerjee, K.; Johnson, Z. T.; Claussen, J. C.; Moudgil, A.; Leong, W. L. Roadmap on Printable Electronic Materials for Next-Generation Sensors. *Nano Futures* **2024**, *8* (3), No. 032001.

(26) Rivnay, J.; Leleux, P.; Ferro, M.; Sessolo, M.; Williamson, A.; Koutsouras, D. A.; Khodagholy, D.; Ramuz, M.; Strakosas, X.; Owens, R. M.; Benar, C.; Badier, J.-M.; Bernard, C.; Malliaras, G. G. High-Performance Transistors for Bioelectronics through Tuning of Channel Thickness. *Sci. Adv.* **2015**, *1* (4), No. e1400251.

(27) Tan, S. T. M.; Lee, G.; Denti, I.; LeCroy, G.; Rozylowicz, K.; Marks, A.; Griggs, S.; McCulloch, I.; Giovannitti, A.; Salleo, A. Tuning Organic Electrochemical Transistor Threshold Voltage Using Chemically Doped Polymer Gates. *Adv. Mater.* **2022**, *34* (33), No. 2202359.

(28) Koutsouras, D. A.; Torricelli, F.; Gkoupidenis, P.; Blom, P. W. M. Efficient Gating of Organic Electrochemical Transistors with In-Plane Gate Electrodes. *Adv. Mater. Technol.* **2021**, *6* (12), No. 2100732.

(29) Cicoira, F.; Sessolo, M.; Yaghmazadeh, O.; DeFranco, J. A.; Yang, S. Y.; Malliaras, G. G. Influence of Device Geometry on Sensor Characteristics of Planar Organic Electrochemical Transistors. *Adv. Mater.* **2010**, *22* (9), 1012–1016.

(30) Liang, Y.; Figueroa-Miranda, G.; Tanner, J. A.; Huang, F.; Offenhaeusser, A.; Mayer, D. Highly Sensitive Detection of Malaria Biomarker through Matching Channel and Gate Capacitance of Integrated Organic Electrochemical Transistors. *Biosens. Bioelectron.* **2023**, *242*, No. 115712.

(31) Nissa, J.; Janson, P.; Berggren, M.; Simon, D. T. The Role of Relative Capacitances in Impedance Sensing with Organic Electrochemical Transistors. *Adv. Electron. Mater.* **2021**, *7* (4), No. 2001173.

(32) Lin, P.; Yan, F.; Chan, H. L. W. Ion-Sensitive Properties of Organic Electrochemical Transistors. *ACS Appl. Mater. Interfaces* **2010**, *2* (6), 1637–1641.

(33) Romele, P.; Ghittorelli, M.; Kovács-Vajna, Z. M.; Torricelli, F. Ion Buffering and Interface Charge Enable High Performance Electronics with Organic Electrochemical Transistors. *Nat. Commun.* **2019**, *10* (1), No. 3044.

(34) Li, T.; Cheryl Koh, J. Y.; Moudgil, A.; Cao, H.; Wu, X.; Chen, S.; Hou, K.; Surendran, A.; Stephen, M.; Tang, C.; Wang, C.; Wang, Q. J.; Tay, C. Y.; Leong, W. L. Biocompatible Ionic Liquids in High-Performing Organic Electrochemical Transistors for Ion Detection and Electrophysiological Monitoring. *ACS Nano* **2022**, *16* (8), 12049–12060.

(35) Wu, X.; Chen, S.; Moser, M.; Moudgil, A.; Griggs, S.; Marks, A.; Li, T.; McCulloch, I.; Leong, W. L. High Performing Solid-State Organic Electrochemical Transistors Enabled by Glycolated Polythiophene and Ion-Gel Electrolyte with a Wide Operation Temperature Range from −50 to 110 °C. *Adv. Funct. Mater.* **2023**, *33* (3), No. 2209354.

(36) Lingstedt, L. V.; Ghittorelli, M.; Lu, H.; Koutsouras, D. A.; Marszalek, T.; Torricelli, F.; Crăciun, N. I.; Gkoupidenis, P.; Blom, P. W. M. Effect of DMSO Solvent Treatments on the Performance of PEDOT:PSS Based Organic Electrochemical Transistors. *Adv. Electron. Mater.* **2019**, *5* (3), No. 1800804.

(37) Tang, K.; Miao, W.; Guo, S. Crosslinked PEDOT:PSS Organic Electrochemical Transistors on Interdigitated Electrodes with Improved Stability. *ACS Appl. Polym. Mater.* **2021**, *3* (3), 1436–1444.

(38) Liang, Y.; Brings, F.; Maybeck, V.; Ingebrandt, S.; Wolfrum, B.; Pich, A.; Offenhäusser, A.; Mayer, D. Tuning Channel Architecture of Interdigitated Organic Electrochemical Transistors for Recording the Action Potentials of Electrogenic Cells. *Adv. Funct. Mater.* **2019**, *29* (29), No. 1902085.

(39) Tian, Z.; Zhao, Z.; Yan, F. Organic Electrochemical Transistor in Wearable Bioelectronics: Profiles, Applications, and Integration. *Wearable Electronics* **2024**, *1*, 1–25.

(40) Sun, H.; Vagin, M.; Wang, S.; Crispin, X.; Forchheimer, R.; Berggren, M.; Fabiano, S. Complementary Logic Circuits Based on High-Performance n-Type Organic Electrochemical Transistors. *Adv. Mater.* **2018**, *30* (9), No. 1704916.

(41) Moudgil, A.; Hou, K.; Li, T.; Leong, W. L. Biocompatible Solid-State Ion-Sensitive Organic Electrochemical Transistor for Physiological Multi-Ions Sensing. *Adv. Mater. Technol.* **2023**, *8* (18), No. 2300605.

(42) Liang, Y.; Ernst, M.; Brings, F.; Kireev, D.; Maybeck, V.; Offenhäusser, A.; Mayer, D. High Performance Flexible Organic Electrochemical Transistors for Monitoring Cardiac Action Potential. *Adv. Healthcare Mater.* **2018**, *7* (19), No. 1800304.

(43) Nielsen, C. B.; Giovannitti, A.; Sbircea, D.-T.; Bandiello, E.; Niazi, M. R.; Hanifi, D. A.; Sessolo, M.; Amassian, A.; Malliaras, G. G.; Rivnay, J.; McCulloch, I. Molecular Design of Semiconducting Polymers for High-Performance Organic Electrochemical Transistors. *J. Am. Chem. Soc.* **2016**, *138* (32), 10252–10259.

(44) Wang, N.; Yang, A.; Fu, Y.; Li, Y.; Yan, F. Functionalized Organic Thin Film Transistors for Biosensing. *Acc. Chem. Res.* **2019**, *52* (2), 277–287.

(45) Wang, Y.; Wustoni, S.; Surgailis, J.; Zhong, Y.; Koklu, A.; Inal, S. Designing Organic Mixed Conductors for Electrochemical Transistor Applications. *Nat. Rev. Mater.* **2024**, *9* (4), 249–265.

(46) Hütter, P. C.; Rothländer, T.; Haase, A.; Trimmel, G.; Stadlober, B. Influence of Geometry Variations on the Response of Organic Electrochemical Transistors. *Appl. Phys. Lett.* **2013**, *103* (4), No. 043308.

(47) Huang, W.; Chen, J.; Yao, Y.; Zheng, D.; Ji, X.; Feng, L.-W.; Moore, D.; Glavin, N. R.; Xie, M.; Chen, Y.; Pankow, R. M.; Surendran, A.; Wang, Z.; Xia, Y.; Bai, L.; Rivnay, J.; Ping, J.; Guo, X.; Cheng, Y.; Marks, T. J.; Facchetti, A. Vertical Organic Electrochemical Transistors for Complementary Circuits. *Nature* **2023**, *613* (7944), 496–502.

(48) Salvigni, L.; Nayak, P. D.; Koklu, A.; Arcangeli, D.; Uribe, J.; Hama, A.; Silva, R.; Hidalgo Castillo, T. C.; Griggs, S.; Marks, A.; McCulloch, I.; Inal, S. Reconfiguration of Organic Electrochemical Transistors for High-Accuracy Potentiometric Sensing. *Nat. Commun.* **2024**, *15* (1), No. 6499.

https://doi.org/10.1021/acsami.6c09414
ACS Appl. Mater. Interfaces XXXX, XXX, XXX−XXX